Evaluating parallax and shadow correction methods for global horizontal irradiance retrievals from Meteosat SEVIRI

Job I. Wiltink[1,2], Hartwig Deneke[3], Chiel C. van Heerwaarden[2], and Jan Fokke Meirink[1]

[1]R&D Satellite Observations, Royal Netherlands Meteorological Institute (KNMI), De Bilt, The Netherlands
[2]Meteorology and Air Quality Group, Wageningen University & Research, Wageningen, The Netherlands
[3]Department of Remote Sensing of Atmospheric Processes, Leibniz Institute for Tropospheric Research, Permoserstraße 15, 04318 Leipzig, Germany

Correspondence: Job I. Wiltink (job.wiltink@knmi.nl)

Abstract.

The transition towards an energy supply with a high share of renewable energy calls for accurate global horizontal irradiance (GHI) observations. Satellite-derived GHI covers large geographical areas, making it an excellent data source for nowcasting solar power generation and the validation of weather and climate models. To obtain a good match between satellite-derived
5 GHI and surface observations of GHI, a precise geolocation of the satellite GHI is an essential factor in addition to the accuracy of the retrieval. The geolocation of satellite retrievals is affected by parallax, a displacement between the actual and apparent position of a cloud, as well as by a displacement between the actual position of a shadow and the cloud casting that shadow. This study evaluates different approaches to correct Meteosat Spinning Enhanced Visible and Infrared Imager (SEVIRI) retrievals for parallax and cloud shadow displacements using ground-based observations from a unique network of 99 pyranometers
10 deployed during the HOPE field campaign in Jülich, Germany, in 2013. The first method provides geometric corrections for the displacements calculated using retrieved cloud top heights. The second method relies on empirical collocation shifting. Here, the collocation shift of the satellite grid is determined by maximizing the correlation between the satellite retrievals and ground-based observations. This optimum shift is determined either based on daily or time step averaged correlations. The time step averaged collocation shift correction generally yields the most accurate results, but the drawback of this method is its reliance
15 on ground-based observations. The geometric correction, which does not have this limitation, achieves the most accurate results if a combined parallax and shadow correction is performed. At higher spatial resolutions, the GHI retrieval accuracy becomes increasingly sensitive to the applied correction. At the SEVIRI standard native resolution of 3×3 km^2 (SR), the root mean square error (RMSE) is reduced by 6.3 W m^{-2} (6.0 %), going from the uncorrected to combined geometrically corrected retrieval. At a threefold higher resolution (HR), this difference increases to 11.7 W m^{-2} (10.8 %). Cloud heterogeneity also
20 strongly influences the sensitivity to geolocation accuracy and spatial resolution. Variable cloud regimes exhibit a higher sensitivity to geolocation corrections compared to less variable regimes. As an illustration, the mean improvement in HR RMSE between the uncorrected retrieval and the time step optimal shift is 13.3 W m^{-2} (10.9%) for the stratocumulus cloud regime, while for the cirrus cloud regime the improvement is negligible.

1 Introduction

Knowledge of the spatial distribution of satellite-derived global horizontal irradiance (GHI) is valuable for multiple reasons, such as in support of the energy transition towards renewable energy sources. Satellite retrievals are widely used for nowcasting GHI and PV power generation (Hammer et al., 1999; Arbizu-Barrena et al., 2017; Ohtake et al., 2018; Wang et al., 2019; Cui et al., 2024) Moreover, GHI retrievals from satellites can be used for the validation of weather and climate models (Freidenreich and Ramaswamy, 2011; Alexandri et al., 2015; Chen et al., 2024). Especially when it comes to km-scale earth system models that start resolving cloud systems, satellite retrievals of clouds and radiation can be of interest.

The first methods to derive GHI from satellites were proposed in the 1960s (Fritz et al., 1964; Vonderhaar and Suomi, 1969). In the late 1970s, the first quantitative estimations of GHI from geostationary satellites were made by Tarpley (1979) using data from the Global Earth Observing System (GOES) satellite (Bristor, 1975). For this first generation of GOES satellites, the pixel resolution was around 8 km at the sub-satellite point. The following decades saw rapid developments in sensor capabilities as well as retrieval algorithms (Huang et al., 2019). Nowadays, geostationary satellites are operated that enable the estimation of GHI down to scales of 500 m (Schmit et al., 2017).

The increase in spatial resolution comes with challenges. One of the challenges for satellite retrievals of GHI is that at higher spatial resolutions the accuracy of the satellite geolocation must be retained to prevent spatial mismatch errors. This is especially important for geostationary imagers observing higher latitudes. At slant viewing angles, scatterers in the atmosphere, in particular clouds, will cause a horizontal shift between the apparent location of the scene from satellite perspective relative to the actual location of the scene when projected vertically at the earth's surface. This is called parallax. It can be calculated using the position of the satellite, the satellite zenith angle and the cloud top height (H_c). In this way, satellite retrievals can be corrected for parallax through a geometric correction. However, the cloud field is retrieved from the satellite measurements, and it contains uncertainties related to the identification of clouds and estimation of H_c. Moreover, the vertical extent of clouds is not considered in the correction, even if it can be highly relevant. Considering clouds and radiation in three dimensions can lead to different surface patterns of GHI (e.g. Gronemeier et al., 2017; Jakub and Mayer, 2017; Veerman et al., 2020). These factors lead to uncertainty in the parallax correction.

As pointed out by Roy et al. (2024-Preprint), several studies report parallax as a source of errors for GHI retrievals (e.g. Perez et al., 2010; Journée et al., 2012; Qu et al., 2017; Harsarapama et al., 2020; Yagli et al., 2020). However, in these studies, a correction for parallax remains omitted. For studies that provide a correction, there is some spread in how the correction for parallax is handled. In Beyer et al. (1996), a geometric correction is implemented for the Heliosat procedure, using a H_c dataset with a spatial resolution of 5×5°. Wyser et al. (2002) implement a parallax correction and apply the correction for every grid cell. Interestingly, they find a limited sensitivity of the accuracy of the GHI retrieval to perturbations in retrieved H_c ($\pm\,25\%$) of simulated cloud fields. In Lorenzo et al. (2017), a Bayesian method is employed that combines satellite-derived GHI with ground observations for optimization of GHI estimates on a city scale. They perform a parallax correction based on a uniform H_c over a $75 \times 80\,\mathrm{km}^2$ area. Parallax correction methods are also applied for the nowcasting of GHI. To prevent the nonphysical breaking of continuous clouds, Miller et al. (2018) first groups adjacent pixels before performing the correction. This cloud

breaking occurs in heterogeneous H_c conditions since higher clouds cause a larger parallax than low clouds. Therefore, after applying the parallax correction, there is a possibility that blank pixels are created where no observations are present since the
60   surrounding clouds obscured these locations.

Correcting satellite retrievals for parallax is not only relevant for GHI retrieval but also for satellite-based rainfall estimations (Bieliński, 2020). However, the difference between parallax corrections for rainfall estimates and GHI is that in the case of GHI, the effect of the cloud shadow location cast by the cloud on the earth's surface needs to be considered in addition. To correct the cloud shadow location, again, a geometric correction can be performed based on cloud location and solar position
65   (azimuth and zenith angle) (Beyer et al., 1996; Wyser et al., 2002; Lorenzo et al., 2017; Miller et al., 2018; Roy et al., 2024-Preprint). Roy et al. (2024-Preprint) demonstrate the relevance of combined parallax and cloud shadow corrections when the sun and satellite are located in the same cardinal direction.

Besides geometric corrections, ground observations can also be used to empirically correct for parallax and shadow displacements. In Deneke et al. (2021) a method is used to correct for parallax primarily aimed at GHI retrievals. The authors
70   apply a collocation shift that is based on the daily mean optimal correlation between the SEVIRI retrievals and a network of 99 pyranometers employed for the 2013 HOPE field experiment that took place from April to July 2013 in Jülich, Germany (Macke et al., 2017). A shortcoming of the daily mean optimal shift method is that the diurnal variation of cloud shadow location is not considered, and only the daily averaged cloud shadow position remains accounted for. Therefore, the accuracy of the correction decreases towards the morning and afternoon (Wiltink et al., 2024).

75   As outlined in the previous paragraphs, multiple studies address methods for correcting parallax and shadow displacements to ensure geolocation accuracy. However, the accuracy of different correction methods, such as the mean optimal shift method and geometric corrections, including their handling of H_c, have not been extensively validated against each other. This study aims to do so by using the 2013 HOPE field campaign data as a reference.

Another goal of this study is to quantify the impact of the applied corrections on the accuracy of GHI retrievals at varying
80   resolutions. Applying parallax and shadow corrections becomes increasingly relevant at higher resolutions (Journée et al., 2012). This is because the same parallax or shadow correction will lead to a shift by more pixels for the higher resolution retrieval. Increased spatial variability at higher resolutions can introduce larger spatial mismatch errors if the corrections are not performed accurately. Finally, the importance of precisely applying parallax and shadow corrections for the GHI retrieval accuracy largely depends on the heterogeneity of the observed cloud deck, with larger errors being observed for partly cloudy
85   conditions (Marie-Joseph et al., 2013). However, to our knowledge, this remains poorly quantified for various cloud regimes. Therefore, in this study, we will assess how the improvement in the accuracy of GHI retrievals as a result of parallax and shadow corrections varies with cloud conditions.

The remainder of this article is structured as follows. Data and used instruments are described in Section 2. Next, in Section 3 the various parallax and shadow correction methods are introduced. Results are shown in Section 4 and discussed in Section
90   5. The conclusions and outlook are provided in Section 6.

2 Data

This study builds upon the same instruments and datasets described in Wiltink et al. (2024). This section recaps the most essential parts of these datasets.

The parallax and shadow corrections are investigated for the 18th of April until the 22nd of July 2013, for a study domain centred around Jülich, Germany. These dates coincide with the HD(CP)^2 Observational Prototype Experiment (HOPE) field campaign (Macke et al., 2017). During this campaign, 99 pyranometers were installed to measure GHI over an area of 10×12 km^2 (50.85-50.95° N and 6.36-6.50°) around Jülich (Madhavan et al., 2016). The original HOPE pyranometer dataset includes quality information based on the manually recorded status and visual checks. An additional quality screening was undertaken to ensure questionable data is omitted from the dataset, explained in more detail in Wiltink et al. (2024). Only the data between 06:15 and 16:45 UTC that has passed quality control is considered. In this study, these pyranometers serve as a reference to evaluate the accuracy of the parallax and shadow corrections applied to the satellite retrievals.

We use spectral reflectances of the Spinning Infrared Imager (SEVIRI; Schmetz et al., 2002) onboard the second generation of Meteosat satellites as inputs to derive GHI. SEVIRI-derived GHI can be computed every 5 minutes using the Rapid Scan Service. SEVIRI operates 11 spectral channels in the visible to infrared range of the spectrum with a spatial resolution of 3×3 km^2. Besides the 11 narrowband channels, SEVIRI has one High-Resolution Visible (HRV) channel with a broader spectral response but an improved spatial resolution of 1×1 km^2 at nadir. Due to slanted viewing angles of SEVIRI, the resolution over the study domain is 6.1×3.2 km^2 or 2.0×1.1 km^2 for the narrowband and HRV channels, respectively. The spatial resolution of the GHI retrieval can be improved from the narrowband resolution (SR) to the HRV resolution (HR) by adopting a downscaling method that links the reflectances of the HRV channel to the spectrally overlapping narrowband channels (VIS006 and VIS008) (Deneke et al., 2021). Until 2017, an erroneous georeferencing offset was contained in the Level 1.5 SEVIRI images. The pixels of the SEVIRI grid were shifted by 1.5 km both in the northward and westward directions (EUMETSAT, 2017), corresponding to shifts of 0.5 SR and 1.5 HR pixels. To ensure accurate georeferencing, we corrected the pixel shift in the SEVIRI grid before the parallax and shadow corrections were performed.

To calculate GHI from SEVIRI reflectances, the CPP-SICCS algorithm (Cloud Physical Properties - Solar Irradiance under Clear Cloudy Skies) (Greuell et al., 2013; Benas et al., 2023) is executed. Besides SEVIRI reflectances, this algorithm relies on additional input. We use the NWC SAF GEO v2021 software package to determine cloud mask, cloud type, cloud top temperature, and H_c (NWC SAF, 2021). The RTTOV v. 13 radiative transfer model (Saunders et al., 2018; Hocking et al., 2021) is used to simulate brightness temperatures under clear and cloudy conditions. NWP reanalysis and forecast data from the Copernicus Atmospheric Monitoring Service (CAMS) (Inness et al., 2019) is retrieved to get information on the atmospheric state. The CAMS data includes temperature and humidity profiles, aerosol properties and the integrated ozone column. Finally, surface reflectances are required, which are taken from the Land Surface Analysis Application Facility LSA SAF: (Carrer et al., 2018).

CPP first determines cloud phase and then uses lookup tables (LUTs) precalculated with the Double Adding KNMI (DAK) model (de Haan et al., 1987; Stammes, 2001) to compute cloud optical thickness (τ) and effective radius (r_e) following the

ID	NWC SAF cloud type	ID	CRAAS regime
1	Cloud-free land	1	Cirrus
2	Cloud-free sea	2	Cirrostratus
3	Snow over land	3	Deep convection
4	Sea ice	4	Alto- & nimbo-type clouds
5	Very low clouds	5	Mid-level clouds
6	Low clouds	6	Shallow cumulus, fog
7	Mid-level clouds	7	Stratocumulus
8	High opaque clouds	8	Fair-weather clouds
9	Very high opaque clouds	9	Clear Sky
10	Fractional clouds		
11	High semitransparent thin clouds		
12	High semitransparent moderately thick clouds		
13	High semitransparent thick clouds		
14	High semitransparent above low or medium clouds		
15	High semitransparent clouds above snow or ice		

Table 1. NWC SAF cloud type ID and CRAAS ID and their corresponding main cloud type/regime.

125 bispectral reflectance method of Nakajima and King (1990). SICCS then takes τ and r_e, along with a new set of LUTs computed with broadband DAK (Munneke et al., 2008) to determine GHI. In addition, SICCS accounts for the effects of aerosols on GHI based on the aerosol properties taken from the CAMS reanalysis for cloud-free pixels.

The ground-based and satellite observations are compared by deriving a SEVIRI time series for each pyranometer station at HR and SR. The scale difference between both types of observations is accounted for by smoothing the SEVIRI retrieval

130 with a Gaussian filter where the Gaussian filter width σ is set to 1.0 km. To match the SEVIRI RSS temporal resolution, the pyranometer network data is averaged to 5-minute intervals. The 5-minute averaging period is centred around the actual acquisition time for the Jülich area, which is about 3 minutes after the start time of the RSS scan.

The parallax and shadow corrections described in the next section require specific input data, including the satellite and solar positions and H_c, which are already available as input or output of the CPP-SICCS retrieval.

135 Finally, the CRAAS cloud regime dataset (Tzallas et al., 2022a) is used to study the dependence of results on cloud conditions. This dataset identifies eight cloud regimes based on joint histograms of τ and cloud top pressure at a $1° \times 1°$ spatial and 15-minute temporal resolution, using k-means clustering to identify these regions. A ninth cloud regime consisting of the ten most persistent clear-sky days of the HOPE-campaign is added here as a separate regime. The regime IDs and associated cloud types are summarized in Table 1. The NWC SAF cloud types are also noted as a reference.

140

3 Methodology

In this section, the geometric corrections for parallax (Sect. 3.1) and shadow displacement (Sect. 3.2) are described. Section 3.3 introduces experiments to test the sensitivity to the use of H_c in these corrections. Finally, in Section 3.4, an empirical geolocation correction method based on the ground-based pyranometer network data is introduced.

3.1 Parallax correction

To correct the SEVIRI retrievals for parallax, we use the Satpy modifiers.parallax version 0.49.0 Python library (Satpy Developers, 2024). Here, the parallax correction is briefly recapped and graphically illustrated in Figure 1. For more details we refer to Satpy Developers (2024) and references therein. The correction starts with the computation of the satellite viewing zenith angle (θ_s). This requires a transformation of the earth-centred inertial coordinate system to a topocentric coordinate system, in which the local observer horizon is used as the fundamental plane. The transformation is achieved by applying two rotations. In the topocentric coordinate system then also the vectorial distance between the satellite and the uncorrected pixel of interest ($\Delta x_{\mathrm{sat2surf}}$, $\Delta y_{\mathrm{sat2surf}}$, $\Delta z_{\mathrm{sat2surf}}$) can be calculated, as well as the corresponding slant distance ($\Delta s_{\mathrm{sat2surf}}$). Then, from H_c, the slant distance between cloud-top and the uncorrected pixel ($\Delta s_{\mathrm{cld2surf}}$) and the parallax distances (Δx_{pllx}, Δy_{pllx}) can be calculated using geometric similarity:

$$\frac{\Delta s_{\mathrm{cld2surf}}}{\Delta s_{\mathrm{sat2surf}}} = \frac{\Delta x_{\mathrm{pllx}}}{\Delta x_{\mathrm{sat2surf}}} = \frac{\Delta y_{\mathrm{pllx}}}{\Delta y_{\mathrm{sat2surf}}} = \frac{H_c}{\Delta z_{\mathrm{sat2surf}}}. \tag{1}$$

Finally, the parallax distances are converted to spherical coordinates, yielding the parallax shift in longitude and latitude ($\Delta \mathrm{lon}_{\mathrm{pllx}}$, $\Delta \mathrm{lat}_{\mathrm{pllx}}$).

3.2 Shadow correction

For accurate retrieval of surface GHI the positioning of the cloud shadow location is highly relevant. The SEVIRI GHI retrieval relies on an assumption of 1-dimensional (1D) radiative transfer. A consequence of this approach is that for the GHI retrieval the cloud shadow is assumed to be directly beneath the cloud. The cloud shadow correction aims to shift the pixel to the actual position of the shadow.

The cloud shadow displacement ($\Delta \mathrm{lon}_{\mathrm{shdw}}$, $\Delta \mathrm{lat}_{\mathrm{shdw}}$) can be computed from the cloud top height (H_c), the solar zenith angle (θ_0), the solar azimuth angle (ϕ_0) and the Earth's radius (R_{earth}), as shown by Equations 2 and 3 and graphically illustrated in Figure 2:

$$\Delta \mathrm{lon}_{\mathrm{shdw}} = \frac{H_c \tan \theta_0 \sin \phi_0}{R_{\mathrm{earth}}}; \tag{2}$$

$$\Delta \mathrm{lat}_{\mathrm{shdw}} = \frac{H_c \tan \theta_0 \cos \phi_0}{R_{\mathrm{earth}}}. \tag{3}$$
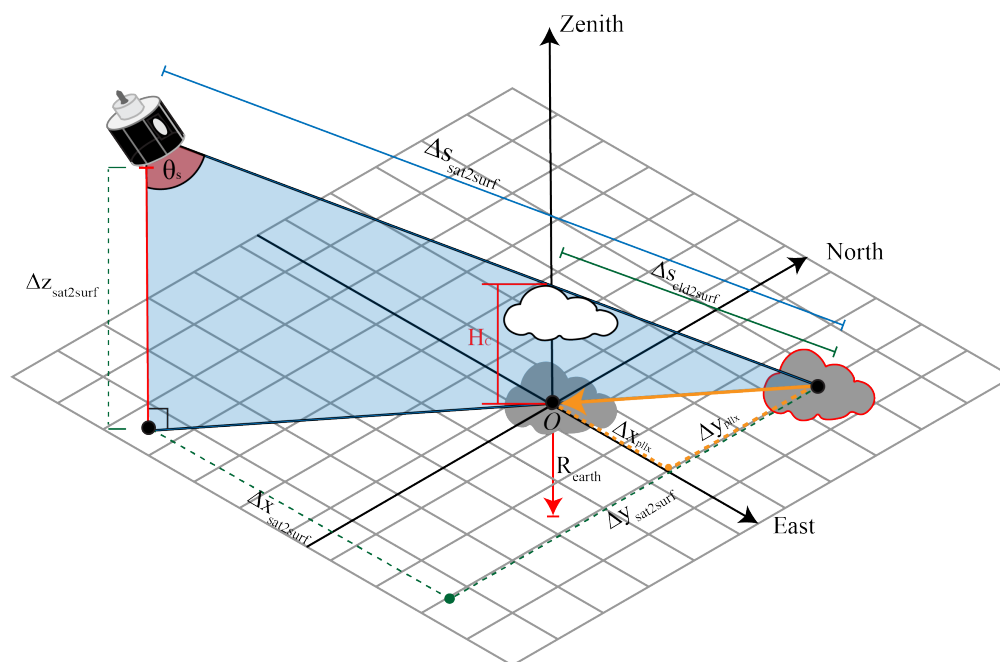
Figure 1. Schematic overview from a topocentric perspective of the positions, angles and distances required to compute the parallax correction. The meaning of the symbols is explained in the text.
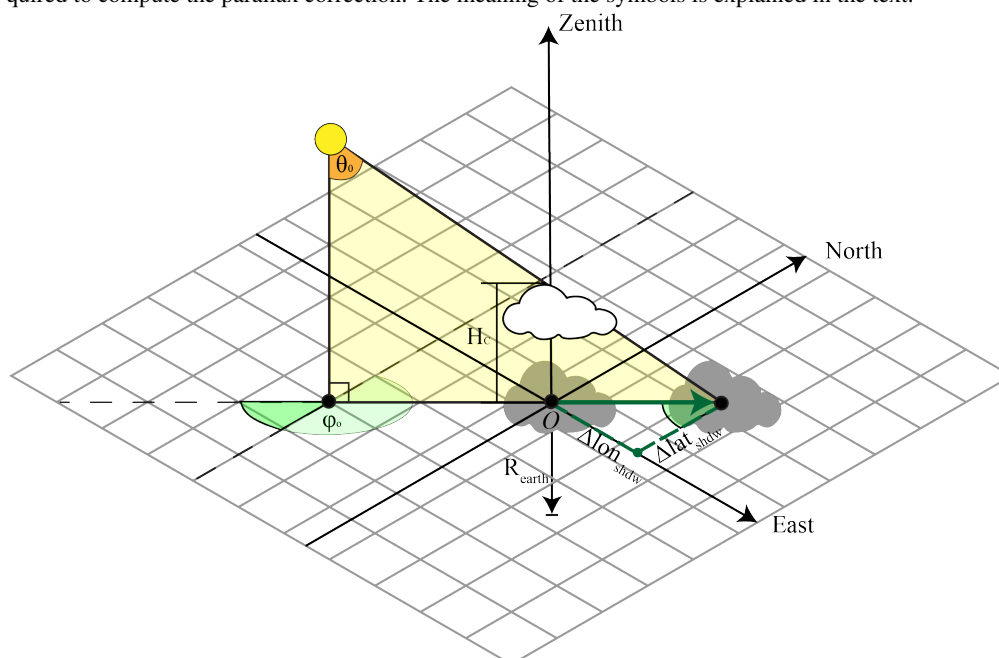

Figure 2. Schematic overview from a topocentric perspective of the positions, angles and distances required to compute the shadow correction. The meaning of the symbols is explained in the text.

3.3 Parallax and shadow correction experiments

Initially, we calculate a parallax and shadow correction for every pixel that has been flagged as cloudy. However, uncertainties

170   in the retrieved cloud mask and H_c can lead to inaccuracies in the magnitude of the applied parallax correction, for instance when pixels are falsely identified as either clear-sky or cloudy. To get an estimate of the effect of these inaccuracies, two additional experiments are performed that evaluate the sensitivity of the parallax and shadow corrections to variations in H_c.

1. In the first experiment, we create a dataset in which the parallax and shadow corrections are calculated using the median H_c value over 55×55 HR or 19×19 SR pixels surrounding the Jülich study domain, which corresponds to an area of

175   about 110×58 km^2. This is termed the area-based approach as opposed to the pixel-based approach.

2. In the second experiment, H_c is reduced in steps of 10% from 100% to 0% relative to its retrieved value, before the computation of the parallax and shadow displacement. Reducing the H_c effectively means that we are reducing the magnitude of the applied corrections. Note that a correction that uses 0% of the retrieved H_c is the same as not performing a parallax or shadow correction. The reduced H_c is referred to as the 'relative H_c' in the remainder.

180   The experiments listed above are performed three times at HR as well as SR. The first time, only a parallax correction is performed. The second time only the shadow position is corrected. Finally, we combine both the parallax and shadow correction by first computing the magnitude of the parallax and then applying the shadow correction to the parallax corrected cloud position.

3.4 Empirical collocation shift correction

185 Besides the geometric correction for parallax and shadow displacement described in the previous subsections, we also use an empirical method to improve the GHI geolocation accuracy. This method relies on optimising the correlation between the GHI measured by the pyranometer network and the GHI from the SEVIRI-derived time series for all the data between 06:15 and 17:15 UTC. The procedure to determine this mean optimal shift method is as follows. For each day of the field campaign, the SEVIRI grid is shifted by multiples of 500 m in any direction, after which the correlation between the SEVIRI GHI and

190 the pyranometer network GHI is calculated. An optimal collocation shift for the whole period of the HOPE campaign is then determined based on the highest mean correlation over all the days. For the HR retrieval this daily mean optimal shift is achieved by moving the SEVIRI grid 3.0 km south and 0.5 km east. For the SR retrieval a nearly identical mean optimal shift of 3.0 km south and 1.0 km east is obtained.

A shortcoming of the daily mean optimal shift method is that the diurnal variation of the shadow position remains unac-

195 counted for. Throughout the day, the optimal collocation shift is not constant. For that reason, a mean optimal shift per time step is also calculated (Fig. 3). To illustrate the diurnal variation in this time step optimal shift, it is computed separately for each week of the field campaign. In Figure 3, small-temporal-scale variations have been smoothed out by applying a rolling mean with a width of one hour to show the general trends of the time step mean optimal shift. The longitude of the optimal shift moves from west to east in line with the shadow position (Fig. 3a). Accordingly, the optimal shift for latitude moves slightly
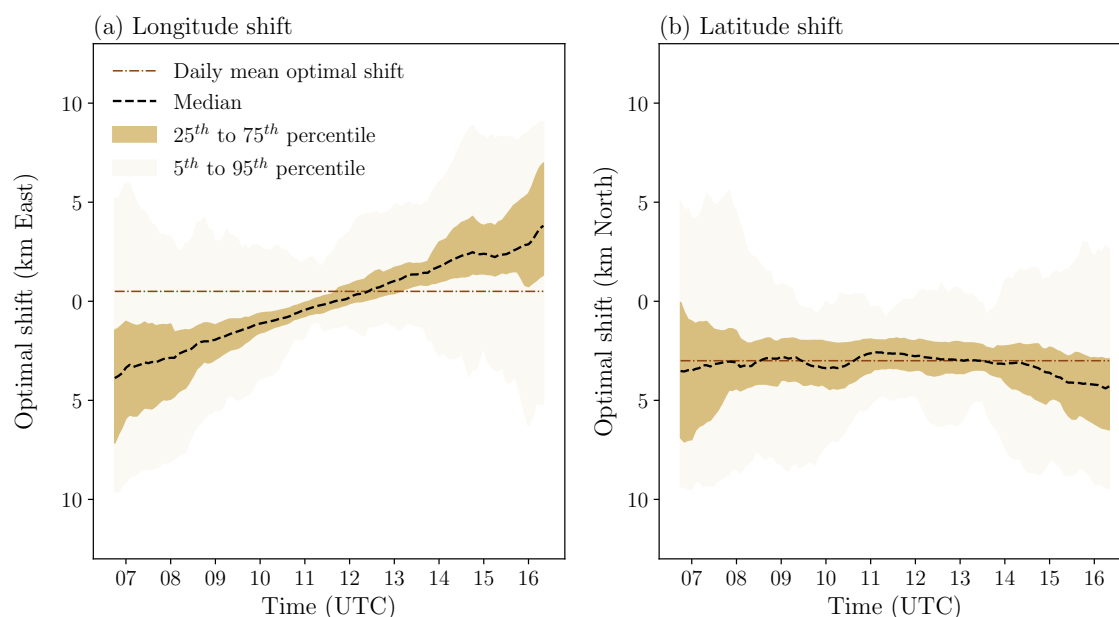
Figure 3. Optimal (a) longitude and (b) latitude shift for the dates of the HOPE field campaign based on the time step mean optimal shift which is computed here from HR retrievals for each week of the field campaign separately. The dashed line shows the median time step optimal shift whereas the shaded areas show the spread in optimal shift between different weeks. The daily mean optimal shift, determined over the full length of the field campaign is indicated by dashed-dotted lines.

northward in the early morning and slightly southward in the late afternoon (Fig. 3b). Especially in the early morning and in the afternoon, the time step mean optimal shift deviates strongly from the daily mean optimal shift.

Figure 3 also indicates the weekly variation of the optimal shift as shown by 25 to 75 and 5 to 95 percentiles. The time step optimal shift depends on solar position and, therefore, is not constant throughout the year. Furthermore, variations in present weather conditions and cloudiness account for some of the observed spread in the week-to-week time step mean optimal shift as well. Especially earlier in the morning and later in the afternoon, an increased variation in optimal shift can be observed compared to noon. Finally, assuming an identical cloud field, with the sun lower in the sky during the morning and afternoon (i.e., larger solar zenith angles), the magnitude of the shadow displacement will be larger than around noon, allowing for an increased range of possible optimal shifts.

To ensure the most robust estimate, the time step mean optimal shift is, in the remainder of this article, determined using all the available data from the field campaign for each specific time step.
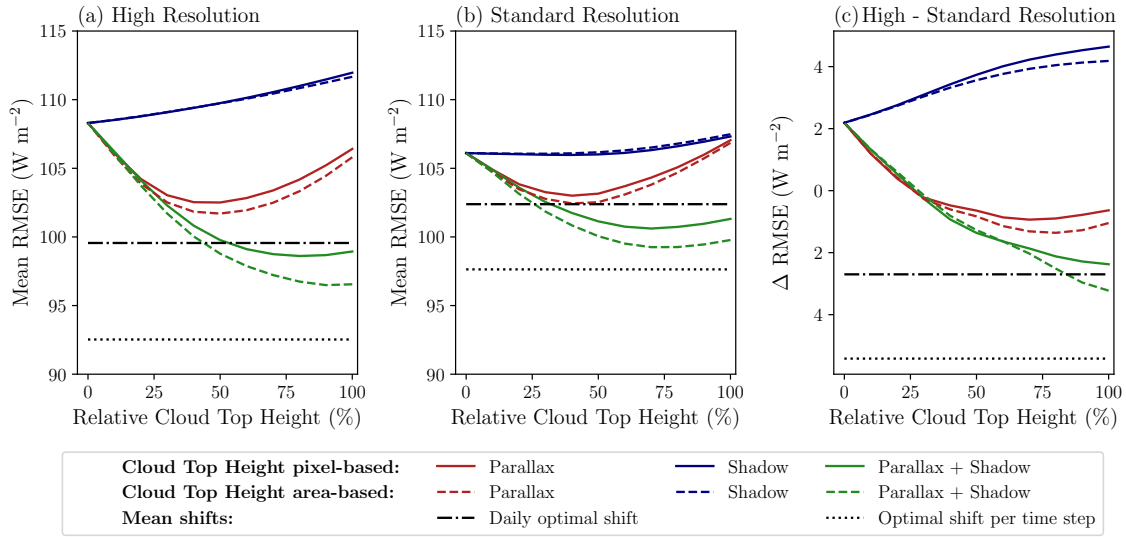
Figure 4. Mean RMSE of GHI with reference to the ground-based observations for various parallax and shadow correction methods as function of relative cloud top height at (a) HR, (b) SR, and (c) difference between HR and SR. In addition to the parallax and shadow corrections the empirically determined daily mean and time step mean optimal shifts are also shown.

4 Results

This section shows the accuracy of GHI retrievals during the HOPE field campaign when various parallax and shadow correction methods are applied. In Section 4.1, the corrections are evaluated for all cloud conditions both at HR and SR. Next, in Section 4.2, the dependence of the effect of the corrections on the cloud regime is quantified in more detail. Finally, in Section 4.3, the diurnal variability in accuracy of the applied corrections is assessed.

4.1 All conditions

Figure 4 shows the mean root mean square error (RMSE) between satellite and ground-based GHI for the parallax, shadow and combined corrections as a function of the relative H_c at HR (Fig. 4a) and SR (Fig. 4b). For both resolutions, also the daily and time step mean optimal shift are shown, which are independent of the relative H_c.

4.1.1 Separate parallax and shadow corrections

We start the analysis by looking into the separate corrections. For the separate shadow correction, the smallest errors are achieved when no correction is performed (i.e., relative H_c is 0). Increasing the relative H_c also increases the mean RMSE. This increase in RMSE could be expected since the shadow correction is performed for the uncorrected, and thus incorrect, cloud position. Therefore, the cloud shadow will be shifted to the wrong position.

10

225   A parallax correction is required to correct the cloud position. If only the parallax correction is performed, we observe a decrease in mean RMSE until a relative H_c of 40-50 %, after which RMSE increases again. Even though only a parallax correction is performed, the cloud shadow position still influences the magnitude of the observed RMSE between the SEVIRI retrieval and the pyranometer network. Therefore, the cloud shadow position still needs to be considered to understand the observed RMSE trend with respect to relative H_c. With the parallax correction, the cloud location is shifted towards the

230   equator (i.e. satellite longitude and latitude). On average, the sun is positioned south of the HOPE field campaign domain and therefore, the cloud shadows will be located north of the clouds. A shift northward is required to correct for the cloud shadow location. Thus, on a daily scale, the directions of the parallax and shadow corrections counteract each other. As a consequence, the optimal parallax shift is achieved when a smaller correction or shift towards the equator is used. For the field campaign, this means that when only a parallax correction is performed, basing this on slightly less than half the retrieved H_c leads to the

235   lowest errors.

4.1.2   Combined parallax and shadow correction

As was already hinted at in the previous paragraph, the optimal geometric correction is achieved when a combination of both parallax and shadow corrections is used. The parallax correction is required to improve the accuracy of the cloud (top) position. A more accurately retrieved cloud position enables the cloud shadow position to be calculated more precisely. Since we are

240   interested in GHI at the surface, the accuracy of the cloud shadow position will be relevant for determining the GHI and its RMSE with respect to the pyranometer network. For the combined geometric correction, the smallest RMSE values are found when it is based on about 70 % to 90 % of the retrieved H_c, depending on the resolution and whether pixel or area-based H_c is used. The smallest RMSE for SR is achieved at a slightly lower relative H_c than for HR. In both cases, however, compared to the full corrections, the improvements in accuracy for the relative H_c values for which the RMSE is minimal,

245   are not statistically significant at a 95 % confidence interval according to the Moods median test (Mood, 1950). Nevertheless, by solely relying on the retrieved H_c for the parallax and shadow corrections effectively, the vertical structure of clouds is disregarded. The parallax and shadow corrections implicitly assume that all scattered radiation originates from the cloud top. However, depending on the cloud's vertical structure, part of the radiation comes from lower altitudes and will have smaller parallax and shadow displacements. Full three-dimensional radiative transfer must be applied to resolve these effects, but the

250   vertical and sub-pixel cloud information to drive such simulations is not available.

4.1.3   Pixel-based and area-based corrections

A comparison of the geometric corrections derived from pixel-based H_c (continuous lines in Fig. 4) and area-based H_c (dashed lines in Fig. 4) shows that the latter results in smaller RMSEs. The difference in accuracy between both methods increases with relative H_c. This could be expected since at higher relative H_c, the corrections become larger and therefore also the spread

255   in corrections for the pixel-based approach compared with the median approach. For the full parallax and shadow correction, there is a significant reduction in RMSE at both resolutions when the correction is performed using area-based H_c instead of the H_c from every pixel. The reduction is 2.4 W m^{-2} (2.5 %) at HR and 1.5 W m^{-2} (1.5 %) at SR. These results suggest

that by applying the median H_c over an area, uncertainties in the H_c retrieval are better accounted for. The separate parallax correction only shows minor differences between the pixel-based and area-based approaches and is only statistically significant

260   at HR between 50% and 90% relative H_c. The separate shadow correction does not show significant differences between the pixel-based and area-based approaches.

4.1.4   Collocation shift corrections

Comparison of the daily mean optimal shift (dash-dotted lines in Fig. 4) against the geometric corrections shows that equally or more accurate results are achieved for the daily mean optimal shift correction than for the separate parallax or shadow cor-

265   rection, regardless the used relative H_c or resolution. However, the daily mean optimal shift is outperformed by the combined geometric correction method when a relative H_c above 50 % at HR and 30 % at SR is used. Remember that the daily mean optimal shift does not account for the diurnal displacement of the cloud shadow location. If the time step mean optimal shift is used (dotted lines in Fig. 4), which does indirectly account for the variation in cloud shadow position, the HR and SR RMSE are reduced by 7.1 W m^{-2} (7.1 %) and 4.4 W m^{-2} (4.3 %) respectively, compared to the daily mean optimal shift. At both

270   resolutions, applying a time step mean optimal shift results in the smallest RMSEs of the evaluated corrections.

4.1.5   Resolution sensitivity

From Figure 4 it can be observed that the mean RMSEs as a function of the relative H_c show comparable trends for HR and SR. However, the HR retrieval exhibits a larger sensitivity to the magnitude of the applied geometric corrections. Without corrections for parallax and shadow displacement, the SR retrieval is more accurate than the HR retrieval. When the relative

275   H_c is increased from the uncorrected to fully corrected retrieval with area-based H_c, the HR RMSE reduces more strongly (11.7 W m^{-2} or 10.8 %) than the SR RMSE (6.3 W m^{-2} or 6.0 %) and becomes more accurate than the SR retrieval (3.2 W m^{-2} or 3.2 %). For the separate parallax correction, we also see a larger sensitivity of the applied correction to relative H_c at HR than at LR. While the minimal RMSE is achieved with a relative H_c around 40-50 %, the HR benefit remains intact also for larger applied parallax corrections (Fig. 4c). When only a shadow correction is performed also a higher sensitivity

280   to the applied correction is shown for HR. But since RMSE increases with relative H_c for the separate shadow correction, as explained in the previous paragraphs, this leads to a larger reduction in HR accuracy.

Finally, the strongest improvements in accuracy between HR and SR are found for the time step mean optimal shift. Here, the mean HR RMSE is 5.4 W m^{-2} (5.5 %) lower than the SR RMSE. The HR resolution improvement for the daily mean optimal shift remains more limited with 2.7 W m^{-2} (2.6%).

285   ## 4.2   Separation into cloud regimes

Since geometric corrections are highly dependent on the type of clouds, the analysis will be further refined using the CRAAS cloud regimes. Figure 5 shows the mean HR RMSE (Fig. 5b) and the difference in RMSE between HR and SR (Fig. 5c) for each of the nine cloud regimes. In the following subsections, the main characteristics of this figure are presented and discussed.
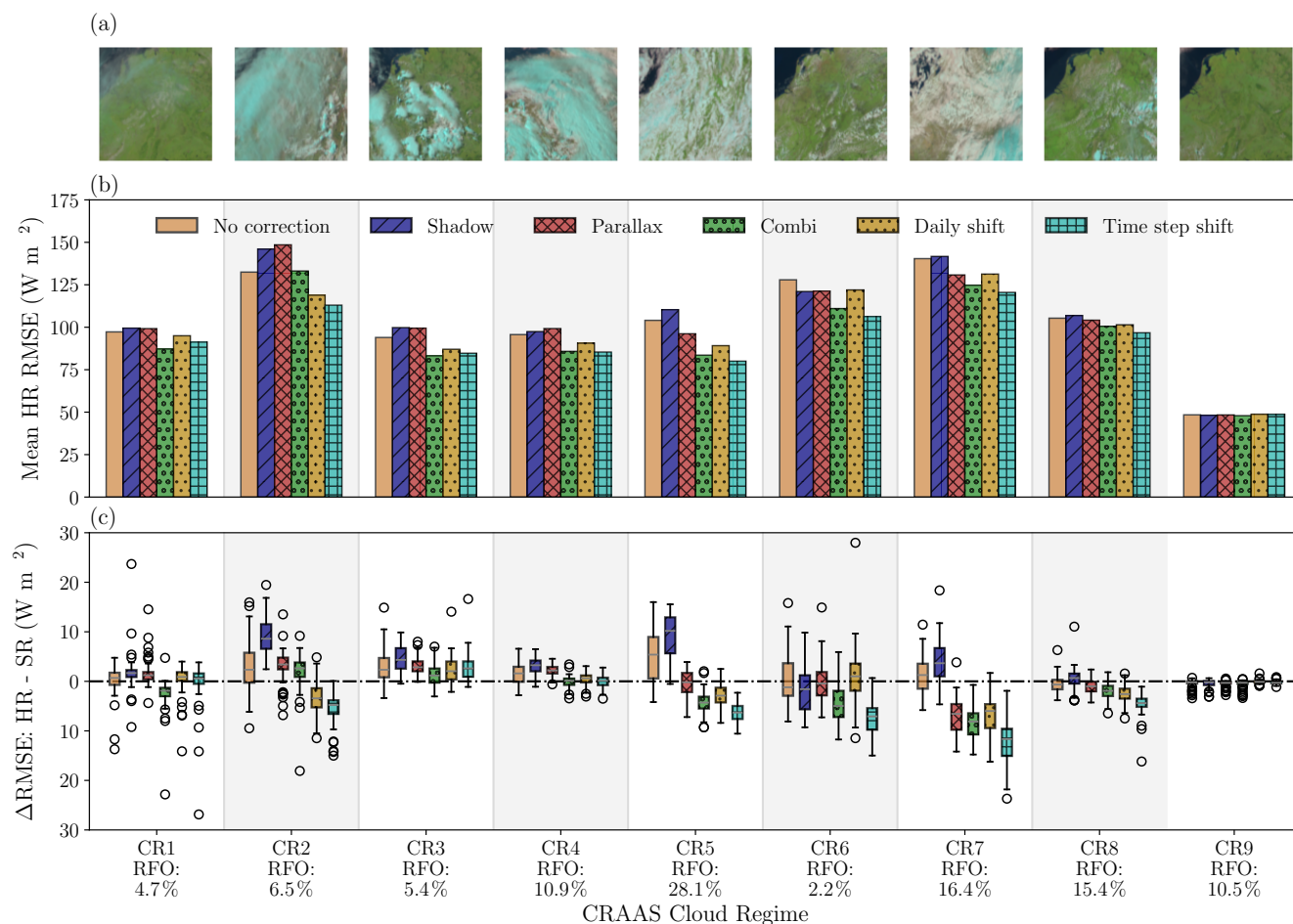
Figure 5. Accuracy of GHI retrieval for different spatial correction methods and separated according to CRAAS cloud regimes: (a) Satpy natural color RGBs of SEVIRI reflectances which are largely representative of each cloud regime; (b) bar charts of the mean RMSE of GHI from the HR retrieval; (c) box-and-whisker plots indicating the HR RMSE improvement (HR – SR). The box-whiskers represent the spread among the 99 pyranometer stations. Full parallax, shadow and combined corrections (relative $H_c = 100\%$) are considered with area-based cloud top height. RFO is the relative frequency of occurrence for each of the 9 cloud regimes.

4.2.1 Regime heterogeneity

290 The first observation from Figure 5b is that the RMSE varies substantially between cloud regimes. As expected, regimes with variable, low clouds (CR6 and CR7) have relatively larger errors, although the cirrostratus regime (CR2) shows comparable errors, which may seem surprising since this cloud type should be quite homogeneous in space and time. However, this finding may be attributed to the frequent occurrence of multilayer clouds with a semi-transparent upper layer and variable clouds below in CR2, as is explained in more detail in Section 4.2.4. The best agreement with ground-based measurements is obtained for

295 clear-sky situations (CR9).

In terms of the different correction methods, a number of general observations can be made. First, the combined parallax and shadow correction performs better than the separate corrections for all cloud regimes. Second, the empirical optimal shift methods yield the best results for the variable, low cloud types (CR5-CR8) as well as CR2, while for the other high-cloud regimes the geometric correction does a better job. Clear-sky situations (CR9) are very homogeneous, and as a result there is

300 no significant difference in RMSE between the various correction methods.

The added value of HR retrievals compared to SR retrievals (Figure 5c) also varies between cloud regimes, and the dependence on the applied correction methods broadly mimics that of the HR RMSE in Figure 5b. In particular, variable cloud regimes such as CR5-CR7, demonstrate a larger spread in HR improvement among the various correction methods compared to less variable regimes such as cirrus (CR1). For instance, for CR7, the difference in mean RMSE improvement (HR-SR)

305 between the time step optimal shift and the retrieval that is not shadow or parallax corrected is 13.3 W m^{-2} (10.9%). For the cirrus cloud regime the difference is negligible with an improvement of only 0.4 W m^{-2} (0.6%). For two cloud regimes the results may appear counter-intuitive. First, the fair weather clouds regime (CR8) can be considered highly variable in space and time. However, this regime includes a considerable number of clear-sky periods during which no difference between HR and SR occurs. As a result the HR-SR improvement as well as the added value of the spatial correction methods remains

310 limited. Second, the cirrostratus regime (CR2) behaves like the variable regimes CR5-CR7 by showing a strong sensitivity of the HR-SR improvement to the correction method. As mentioned before, this may be explained by the presence of multilayer clouds (see Section 4.2.4).

4.2.2 Daily versus time step mean optimal shifts

A general observation in Figure 5b is that for all regimes, the HR RMSE of the time step mean optimal shift is smaller than

315 that of the daily mean optimal shift. Again, the magnitude of the improvement between these two correction methods seems to depend on the variability of the cloud regime. The improvement between daily mean and time step mean optimal shifts is largest for the variable regimes (CR5-CR7) and remains limited for the less variable regimes (e.g. CR1 and CR3).

This can be explained in the following way. For more homogeneous cloud conditions (CR1 and CR3), radiation at the surface will also be spatially more homogeneous, and therefore, the exact shadow position is less relevant. As a result, the influence of

320 a slightly different longitude and latitude shift on the observed RMSE is small. Consequently, this leads to smaller differences between the daily mean and time step mean optimal shift.

The shallow cumulus regime (CR6) best illustrates the advantage of considering a time step mean optimal shift rather than applying a daily mean optimal shift. The mean HR RMSE of the former is 15.6 W m^{-2} (13.0 %) lower than that of the latter. Interestingly, the box-and-whiskers plots for the shallow cumulus regime reveal that when applying the daily mean shift no improvement is obtained from HR compared to SR retrievals, and the resolution improvement only manifests itself when the time step mean optimal shift is considered, although the combined geometric correction also does a good job.

4.2.3 High clouds

As mentioned before, for the more homogeneous regimes with, on average, higher retrieved cloud tops (CR1 and CR3), the combination method of shadow and parallax correction is the most accurate of all applied corrections. This is in contrast to the results for the other regimes (except the clear sky regime), and the integrated results over all the dates of the field campaign, for which the time step mean optimal shift is the most accurate of the correction methods. The combined geometric parallax and shadow corrections for CR1 and CR3 are 4.0 W m^{-2} (4.6 %) and 1.5 W m^{-2} (1.8 %), respectively, more accurate than the time step mean optimal shift method. However, only for the cirrus cloud regime this difference is statistically significant at 95 % confidence interval.

Because of the higher retrieved H_c for CR1 and CR3, the magnitude of the geometrically applied parallax and shadow correction will also be larger compared to the regimes with lower retrieved clouds. In contrast, the mean shift method is based on the optimal shift estimated over all dates of the field campaign, including days with low clouds, days that are predominantly clear-sky, or highly variable in terms of cloud conditions. Variable cloud conditions strongly influence the selected mean optimal shift. This is because, under variable conditions, the computed correlations for each of the shifts vary more strongly compared to more homogeneous situations. In other words, the optimal shift is mainly optimal for the more variable regimes with lower retrieved clouds and, therefore, slightly less optimal for the more homogeneous regimes with higher retrieved clouds. This effect can explain why for CR1 and CR3 the geometric combined parallax and shadow correction is slightly better than the time step mean optimal shift. To a lesser extent, the same reasoning could also be used for CR4, mainly consisting of alto- and nimbo-type clouds. For this regime, the time step mean optimal shift is slightly more accurate than the combined geometric correction but the difference is not statistically significant.

4.2.4 Multilayer clouds

The reasoning of the previous paragraph does not hold for the cirrostratus regime (CR2), which is also a regime with high clouds. Further inspection of this regime using NWC SAF cloud types indicates a high degree of transparency. For around 20 % of observations, multilayer clouds are observed (NWC SAF cloud type 14, see Fig. 6). For these multilayer clouds, the parallax and shadow correction are performed based on the high clouds, while the effect of the underlying clouds on GHI at the surface is likely larger. Because of the high clouds, the applied parallax and shadow correction will be too large for the underlying clouds, leading to larger errors. This issue does not play a role for the mean optimal shifts since the applied mean shift is determined based on all the dates of the field campaign, leading to a smaller applied correction that better fits the
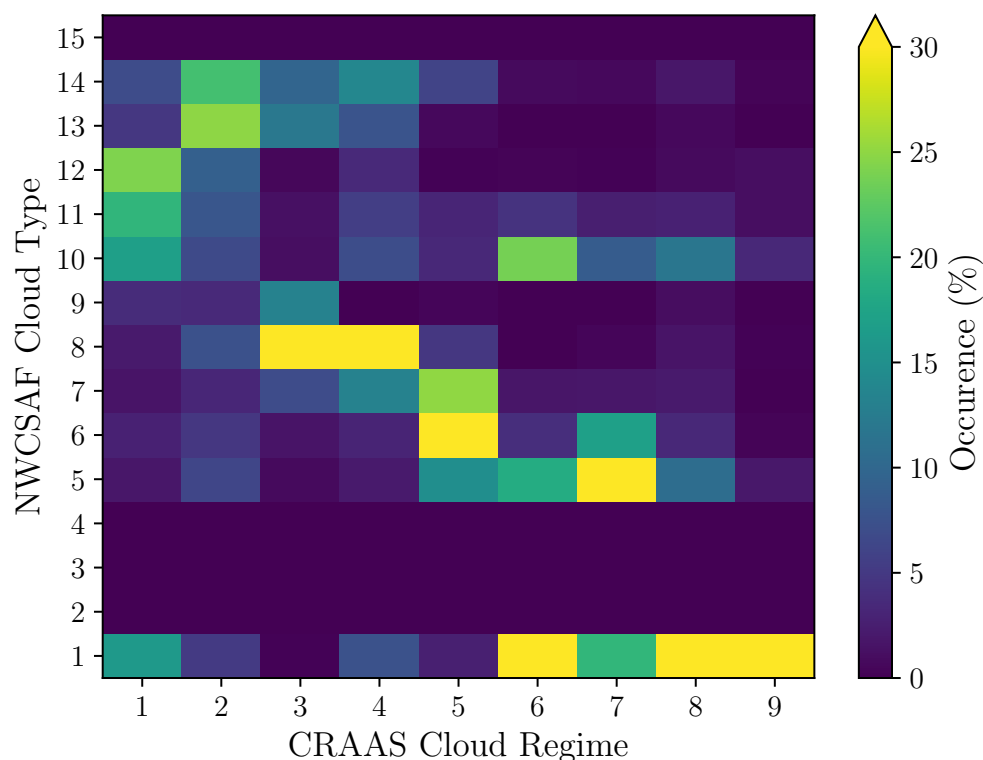
Figure 6. Relative frequency of occurrence of NWC SAF cloud types per CRAAS cloud regime. The complete names of the CRAAS regimes and NWC SAF cloud types with their corresponding IDs are noted in Table 1.

correction required by the underlying clouds. This regime illustrates that applying a geometric parallax and shadow correction,

355 which is solely based on cloud position and H_c information, is challenging in the case of multilayered clouds.

To underline these findings, Figure 7, shows box-and-whisker plots of the RMSE at HR and SR as a function of the relative H_c for the cirrostratus cloud regime. The results of Figure 7 are based on the the combined parallax and shadow correction using the area-based H_c. The median H_c. of the cirrostratus regime for each of the relative H_c bins are shown by the bar charts.

The box-and-whisker plots show that applying a full parallax and shadow correction offers little advantage for the cirrostratus

360 cloud regime. In fact, the uncorrected retrieval produces slightly more accurate results than the fully combined correction. However, at both resolutions, these differences are not statistically significant. Furthermore, for both the fully and uncorrected retrievals, the RMSE is smaller at SR than at HR but again, the difference is not statistically significant.

Still, the geolocation accuracy for the cirrostratus regime can be improved by applying a reduced geometric correction. For the HR retrieval, the smallest RMSE is found using a relative H_c of 40 %, corresponding to around 4000 m. At this relative

365 H_c, the combined geometric correction outperforms the daily mean optimal shift (compare with Fig. 5b), and the HR retrieval is also significantly better than the SR retrieval.
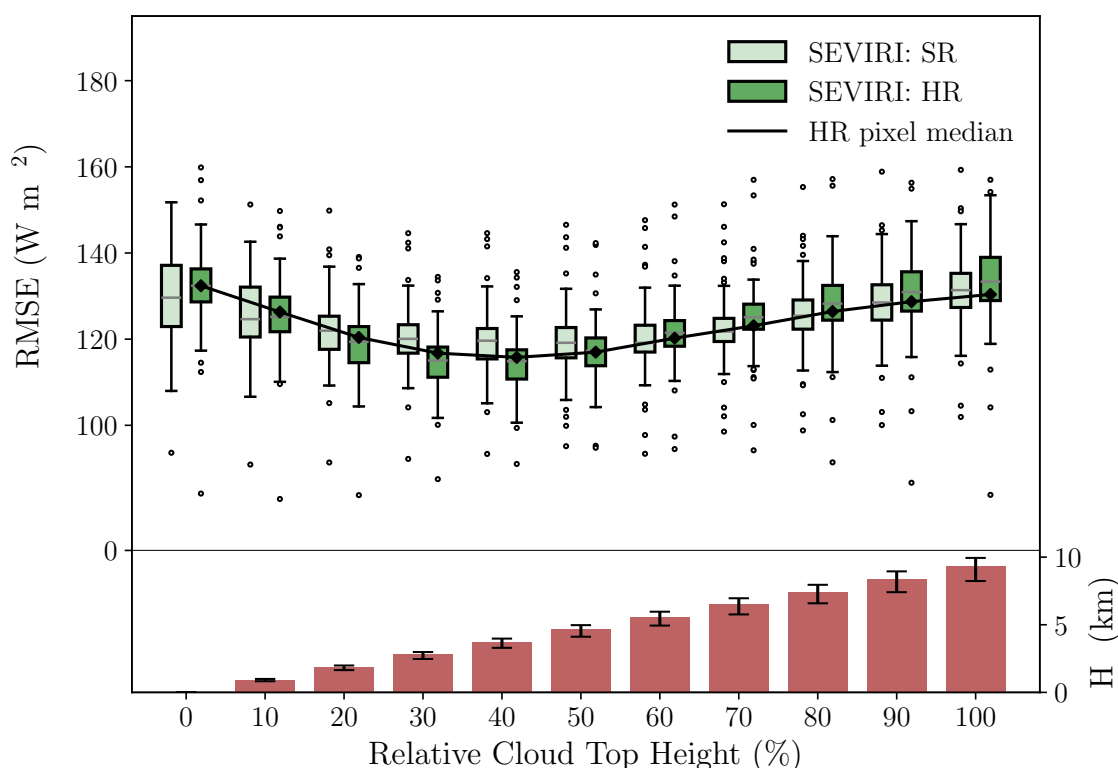
Figure 7. Box-and-whisker plots for the HR and SR RMSE for the combined geometric correction as function of the area-based relative H_c (cloud top height) for the cirrostratus cloud regime (CR2). The black continuous line represents the median RMSE using the pixel-based relative H_c. The median relative H_c in km is shown by the bar chart in the lower panel, in which the markers show the range between the 25th and 75th percentile.

The black line in Figure 7 illustrates the median RMSE for the cirrostratus regime from the pixel-based H_c correction. The trend with relative H_c is comparable to the area-based H_c method. However, the largest differences between both methods occur at full parallax and shadow correction. In the case of a full correction, the pixel-based approach results in a smaller median RMSE. For this regime, the pixel-based approach is likely a better way to handle the retrieved variability in H_c that occurs for multilayer clouds. For all other cloud regimes the area-based method is more accurate than the pixel-based approach for all values of relative H_c (not shown).

4.3 Diurnal cycle

In Figure 8 the relative mean HR RMSE (Fig. 8a) and the HR improvement (Fig. 8b) divided into hourly bins are displayed. The division into hourly bins shows a diurnal cycle with the smallest errors for the time blocks between 8:15 and 11:10 UTC and increasing errors more towards the morning or afternoon (Fig 8a). Note that here the relative RMSE has been plotted
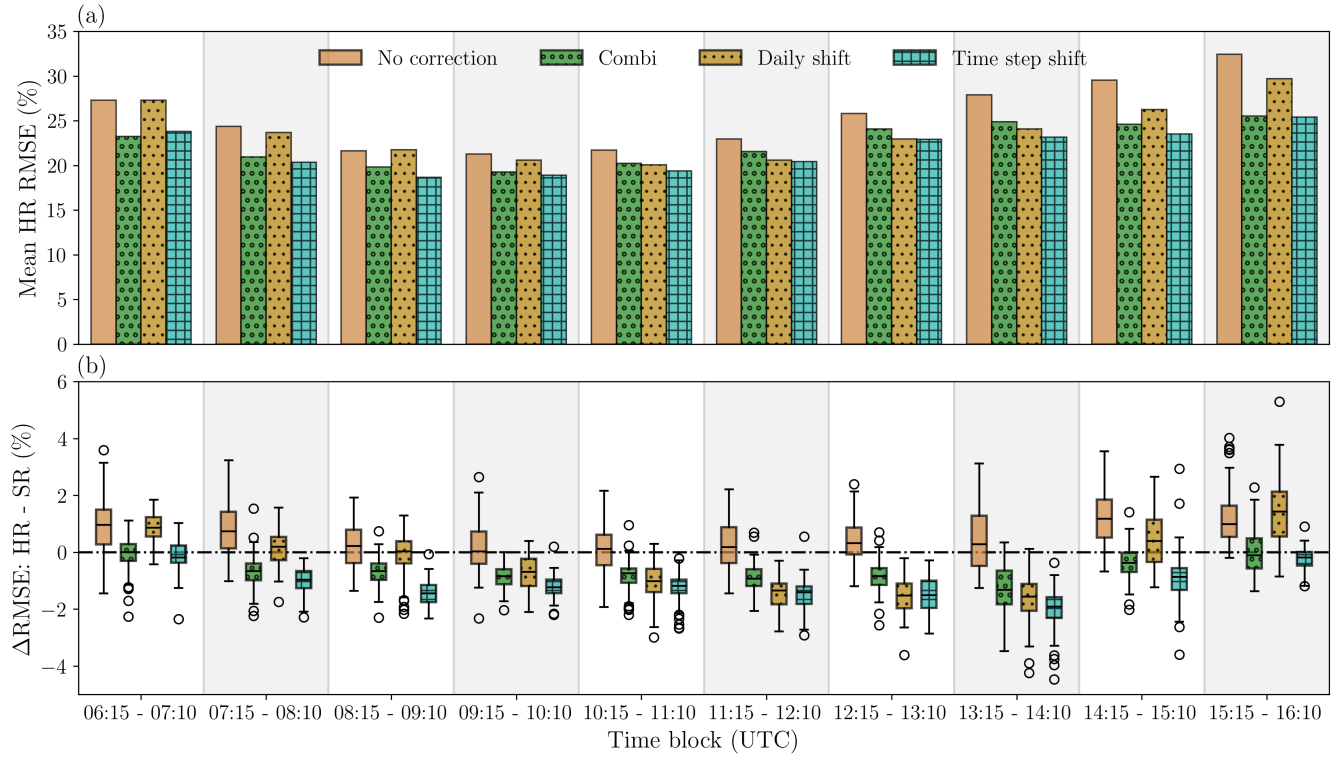
17

Figure 8. Diurnal cycle of GHI retrieval accuracy for different spatial correction methods: (a) bar charts of the mean relative RMSE of GHI separated based on the time of day, in hourly blocks; (b) box-and-whisker plots indicating the relative HR RMSE improvement (HR – SR), again as function of the time of day. Combi refers to the combined parallax and shadow corrections, which have been calculated for area-based relative H_c = 100 %.

to better compare the various time slots. In terms of absolute error the RMSE usually peaks around solar noon when GHI maximizes. The increase in relative RMSEs for the first and last time blocks compared to those on the middle of the day is expected as larger solar zenith angles cause an increased uncertainty in the retrieval. Still, for the time step mean optimal shift and combined geometric correction method, the diurnal variation in RMSE remains more limited when compared to the uncorrected or daily mean optimal shift retrieval. This effect can be explained when the diurnal variation in cloud shadow position is considered. Both with the combined geometric correction and the time step mean optimal shift method the diurnal variation in solar position, and thus shadow location, is accounted for. The daily mean optimal shift only considers the daily averaged cloud shadow position which approximately resembles the situation around noon but does not represent the cloud shadow position in the early morning or late afternoon well. Hence, there is an increase in RMSE for the first and last time blocks while around solar noon the difference between the various methods remains more limited.

Another observation made from Fig. 3a is that towards the afternoon errors are larger than in the morning. This is possibly due to variations in the diurnal occurrence of clouds types. Since convectively driven clouds are more likely to develop in the

18

afternoon (Grabowski et al., 2006), it might lead to increased retrieval errors for those time blocks. Although modest diurnal
390 variations in the relative occurrence of different CRAAS cloud types and the corresponding RMSE are present, we have not
been able to pinpoint theasymmetric diurnal cycle in total RMSE to these variations.

Analysis of the diurnal variation in the magnitude of the HR improvement compared to SR (Fig. 8b) shows that the largest
improvements occur in the afternoon from 13:15 to 14:10 UTC. The diurnal variation in HR improvement is largest for the
daily mean optimal shift method. In the period from 9:15 to 14:10 UTC its median HR RMSE is smaller than the SR RMSE,
395 while for the remaining time blocks the SR retrieval gives more accurate results. The combined geometric correction and the
time step mean optimal shift methods both yield HR improvements at nearly all times of the day. From these two methods, the
time step mean optimal shift produces the largest HR improvements. Remarkably, without spatial correction, the HR retrieval
is outperformed by the SR retrieval throughout the entire day. Overall this illustrates the growing importance of accurate
geolocation at increasing spatial resolutions.

5 Discussion

This discussion section elaborates on the generalizability of the results for other regions or periods (Sect. 5.1). Next, mismatch
or representativeness errors between the SEVIRI retrieval and ground-based observations are discussed, which remain after the
application of the parallax and/or shadow correction (Sect. 5.2).

5.1 Generalizability of results

405 The results presented in this study are valid for a limited domain in the mid-latitudes. Both the geometric correction method
and the collocation shift method, which does require ground observations, can be applied globally. However, the relevance of
the corrections will vary depending on the location, time of day and day of year. This section discusses the generalizability of
our results to other geographical areas.

First, we focus on the parallax correction. Due to the fixed position of geostationary satellites above the equator, the satellite
410 zenith angle increases with increasing latitude. This means that the magnitude of the north-south parallax increases with
latitude, and the effect of parallax on the retrieval accuracy will, therefore, remain more limited compared to higher latitudes.
On the other hand, the location of the current study has almost the same longitude as the Meteosat satellite. For regions at
longitudes that are further apart from the satellite longitude, the east-west parallax will be larger and thus have more impact on
the retrieval accuracy.

415 The second aspect that needs to be considered is the solar position and its effect on cloud shadow location. The solar
position is described by the solar zenith and azimuth angles. The diurnal and seasonal variations of these angles is such that
cloud shadow displacements are smallest around noon and in summer, when the sun is high in the sky. In the early morning and
late afternoon, as well as during winter, cloud shadow displacements are larger and spatial corrections are more relevant. In
terms of geographic location, the overall magnitude of cloud shadow displacements is smallest near the equator and increases
420 toward higher latitudes. However, near the equator the variation in solar azimuth angle still causes a strong diurnal cycle in

east-west cloud shadow displacement, and corresponding corrections are required. Roy et al. (2024-Preprint) assess parallax and cloud shadow corrections for locations with varying latitudes and longitudes, and show that overall larger reductions in the RMSE of satellite-observed GHI against ground-based measurements are obtained for higher θ_s.

Thirdly, regional variations in cloud occurrence are highly relevant in assessing the generalizability of the results. For instance, subtropical land regions, the climatological mean total cloud fraction is very small (Karlsson and Devasthale, 2018), making parallax or shadow corrections to a large extent obsolete. As shown in this article, the importance of the parallax and shadow correction depends on the cloud regime through cloud heterogeneity and cloud top height. In Tzallas et al. (2022a), the annual and diurnal variability of cloud regimes was investigated for Europe. The authors show, for instance, that the fair weather clouds regime is mainly present in summer, while the alto- and nimbo-type clouds are mainly observed during wintertime. Another example is the shallow cumulus regime, which mainly has an oceanic character and therefore will weigh heavier on the overall retrieval accuracy over ocean domains than it does for the Jülich domain in the present study.

Finally, our results show the limitations of the applicability of the geometric correction for multilayered clouds, which, based on the satellite retrievals during the field campaign, mainly occurred in the cirrostratus cloud regime. Li et al. (2015) quantified how the probability of occurrence of multilayer clouds depends on cloud type and latitude. These findings are relevant to assess the utility of the applied corrections at different locations. The statistical evaluation by Li et al. (2015) shows that high clouds, altostratus, altocumulus, and cumulus often coexist with other cloud types. Stratus, nimbostratus, and convective clouds are more likely to occur without other cloud types being present. The observation that high clouds tend to coexist with other clouds agrees well with the high degree of multilayer clouds observed in the cirrostratus cloud regime in this study. Furthermore, the limited occurrence of multilayer clouds for the stratocumulus regime can also be observed in Figure 6. On the other hand, no large degree of multilayer clouds are observed for the cumulus regime in this study. This might be explained by the limitation of passive sensors like SEVIRI to distinguish different cloud levels, for instance, when optically thin cirrus appears above thick shallow cumulus. Multilayer clouds can be much better captured by the active sensor measurements from CALIPSO and CloudSat used by Li et al. (2015). In terms of latitudinal variation, the fraction of multilayer clouds peaks in the tropics, while it has a dip in the subtropics and further minor peaks at mid-latitudes (Li et al., 2015). This suggests larger uncertainties due to parallax and shadow corrections in the tropics. However, effects due to the presence of multilayer clouds are counteracted by the overall smaller parallax and shadow displacements at lower latitudes, as discussed before.

In summary, the impact of spatial displacements on the accuracy of satellite-retrieved GHI is influenced by various factors, and varies in space and time. Overall, this impact increases towards higher latitudes, but the predominant cloud types play an important role as well. We expect that the results of this study in terms of cloud type dependencies are relatively general. However, the magnitude of parallax and shadow displacement effects on GHI remains location-specific.

5.2 Remaining mismatch errors

This paper focuses on spatial corrections for parallax and cloud shadow displacement in order to ensure accurately geolocated GHI retrievals. In theory, the error due to parallax and shadow displacement can be fully accounted for if the clouds are spatially homogeneous objects of which the position is precisely known. However, this is in reality not the case, and further-

455   more, additional mismatch or representativeness errors are introduced when the satellite retrievals are validated against ground observations (Urraca et al., 2024).

A first mismatch error is the result of variations in the spectral range between SEVIRI and the pyranometers of the HOPE network. The spectral differences between SEVIRI and the pyranometer network are mainly at the wavelengths where limited solar radiation is received. Therefore, the magnitude of this error is negligible compared to the temporal and spatial mismatch

460   (Urraca et al., 2024).

Secondly, there are temporal mismatch errors. In this study, the pyranometer data is averaged over a 5-minute time interval centered around the SEVIRI acquisition time. This should reduce the mismatch error, but the error increases with cloud variability and, therefore, will be relevant for heterogeneous cloud conditions.

A third error source is the spatial mismatch. The SEVIRI observations are representative of an area larger than the pixel size,

465   with decreasing sensitivity towards the edges, as governed by the modulation transfer functions of the channels (e.g., Deneke and Roebeling, 2010). The pyranometer measurements are point measurements but since the diffuse radiation originates from the surroundings, they reflect atmospheric conditions in an area. The purpose of the temporal averaging of the pyranometer data is to partly compensate for the spatial point-versus-area mismatch with the satellite observations (Greuell and Roebeling, 2009). In addition, a Gaussian smoothing with a filter width of 1 km is applied to the satellite observations. However, the optimal filter

470   width depends on cloud heterogeneity and, therefore, is not constant between cloud conditions as was demonstrated by Wiltink et al. (2024). Thus, even with this careful collocation and averaging strategy, some uncertainty due to spatial mismatch does remain.

Higher resolution retrievals should be able to better capture the smaller scale variability in GHI around the pyranometer stations, leading to a reduced spatial mismatch error. However, the smallest scale cloud variability will be too fine to be

475   captured by current geostationary satellites. This sub-pixel cloud variability therefore, remains a source of errors leading to biased cloud property retrievals (e.g., Marshak et al., 2006; Zhang et al., 2012; Fu et al., 2022; Matar et al., 2023). Still, biases are generally small if pixels are overcast, but grow rapidly if cloud heterogeneity increases (Zinner and Mayer, 2006).

Finally, 3-dimensional (3D) radiative effects, not included in the SEVIRI retrieval, can introduce a spatial mismatch as well. Furthermore, these 3D effects might limit the accuracy of geometric parallax and shadow corrections, for instance, when it

480   comes to cloud-side illumination. From a 1D perspective, radiation will always enter a cloud from the cloud top. With 3D radiative transfer, this assumption does not hold anymore. A consequence of side illumination is cloud shadow enlargement at the surface. Moreover, since the geometric corrections are based on cloud top height, the magnitude of the shadow corrections is likely overestimated due to side illumination. This effect might partially explain why, for the combined geometric corrections, the lowest RMSE is found below 100 % relative H_c.

485   For the mean optimal shift method, it can be argued that the sub-pixel variability and 3D radiative effects have a smaller influence on the accuracy of the achieved geolocation. The GHI patterns observed by the pyranometer network result from 3D cloud radiation interactions. Since the mean optimal shift method is based on a collocation shift, which optimises the correlation with respect to ground observations, implicitly, the 3D effects, like cloud shadow enlargement, are accounted for.

6 Conclusions and outlook

490 This study evaluates approaches that provide corrections for cloud parallax and shadow displacement to ensure accurate geolocation for GHI retrievals from Meteosat SEVIRI. The assessed approaches include geometric corrections for either parallax, the shadow position or the combination of both. In addition to these geometric corrections an empirical collocation shift method is evaluated. With this method the SEVIRI grid is shifted in longitude and latitude directions, and for each shift the correlation is computed with respect to a network of 99 pyranometer observations employed during the 2013 HOPE field campaign. The

495 optimal shift is then determined as the shift that maximizes the correlation between the SEVIRI retrievals and the pyranometer measurements. The optimal shift is either determined for all data (daily mean optimal shift) or separately for every time slot during the day (time step mean optimal shift). All corrections are performed for SEVIRI retrievals at nadir pixel sizes of 3×3 km^2 (SR) as well as 1×1 km^2 (HR).

For the geometric corrections, at both resolutions, optimal results are found when a combined parallax and shadow correction

500 is performed. If only a shadow correction is performed, the accuracy of the retrievals is not increased. This is due to the shadow correction being applied to a cloud position that has not been parallax-corrected. Meanwhile, the accuracy of a separate parallax correction depends on the cloud top height used to calculate it. For both resolutions, the lowest RMSE of the satellite-retrieved GHI is found if 40-50% of the original, retrieved H_c is used. By only performing a parallax correction, the cloud shadow position is not explicitly considered. However, in many cases, the direction of the cloud shadow displacement (away from the

505 equator) is opposite to the direction of the parallax correction (towards the equator). These opposing effects explain the higher observed accuracy if the separate parallax correction is only performed partially.

Compared to the combined parallax and shadow correction, the geolocation accuracy is further enhanced with the time step optimal shift method. On the other hand, the accuracy of the daily mean optimal shift method is lower than the combined geometric correction. The reason is that the diurnally varying direction of the cloud shadow displacement cannot be captured

510 by a daily mean shift. It should be stressed that, unlike the geometric correction methods, both optimal shift methods require the availability of ground-based observations for their derivation and cannot be applied for an arbitrary location.

The way the retrieved H_c is used for the calculation of the geometric corrections influences the final accuracy. As mentioned before, higher accuracies may be obtained if a lower value than the retrieved H_c is taken. The combined geometric correction, at both HR and SR resolutions, reach the lowest RMSE if they are based on a relative H_c of 70-90%, although RMSE differences

515 with the full corrections are not statistically significant. Furthermore, our results show that the RMSE of retrieved GHI is smaller if an area-based H_c is used instead of single-pixel values. If a full correction is performed, these differences are 2.4 and 1.5 W m^{-2} for HR and SR, respectively.

Corrections to ensure geolocation accuracy become increasingly relevant at higher spatial resolutions. At higher resolutions, finer spatial scales can be resolved, and as a consequence, a slight spatial mismatch can lead to larger errors in retrieved GHI

520 compared to lower resolutions with less resolved spatial variability. The combined geometric shadow and parallax correction best illustrates this. Without any corrections, the SR retrieval gives a smaller RMSE than the HR retrieval. However, if a full combined geometric correction is applied, the HR RMSE reduces more strongly than the SR RMSE. Using the area-based

H_c these reductions are 11.7 W m^{-2} (10.8 %) and 6.3 W m^{-2} (6.0 %), respectively. As a consequence, the full combined geometric correction is 3.2 W m^{-2} (3.2 %) more accurate at HR than at SR.

525   Additionally, the importance of the corrections is influenced by the heterogeneity of the present cloud conditions. The categorization of cloud conditions into cloud regimes underlines that applying parallax and shadow correction is much more relevant for variable cloud regimes, especially at higher resolutions. These conclusions are based on the observed spread in HR improvement (HR - SR RMSE) among the various correction methods. The mean HR RMSE improvement between the uncorrected retrieval and the time step mean optimal shift retrieval is 13.3 W m^{-2} (10.9%) for the variable stratocumulus
530   regime while for the less variable cirrus regime this improvement is negligible.

The division into cloud regimes also highlights the limitations of the applicability of the geometric correction for multilayered clouds In the dataset used for this study, the cirrostratus cloud regime exhibits a considerable fraction of multilayer clouds of around 20 %. For this regime, the full geometric correction is less accurate than the uncorrected retrieval at both resolutions. This is the only regime for which this is the case. The reduced accuracy for this regime is explained by the magnitude of the
535   applied correction. Because of the presence of high clouds, the applied correction is too large for the underlying clouds, which have a more pronounced effect on GHI at the surface.

This study shows the relevance of accurately correcting GHI retrievals for parallax and shadow displacement at increasing resolutions. With SEVIRI the maximum spatial resolution that can be achieved is 1×1 km^2 at nadir. The current generation of geostationary satellites like the GOES Advanced Baseline Imager (GOES ABI; Schmit et al., 2017) and the Meteosat Third
540   Generation Flexible Combined Imager (MTG-FCI; Holmlund et al., 2021) enables retrievals of GHI down to scales of 500 m. However, it is not yet clear what the effect of these improved resolutions on the accuracy of GHI as well as the parallax and shadow corrections will be. New measurement campaigns like the "Small-Scale Variability of Solar Radiation" (S2VSR) field campaign (Deneke et al., 2024) at the ARM Southern Great Plains observatory can provide these insights. With observations from this campaign, the accuracy of the parallax and shadow corrections for modern geostationary satellites can be assessed.

545   Finally, towards higher resolutions 3D radiative transfer effects become increasingly important. The current retrievals of cloud properties and GHI are based on 1D radiative transfer, assuming spatially homogeneous clouds and pixels that are radiatively independent from each other. These assumptions may lead to large cloud and GHI retrieval biases (e.g., Marshak et al., 1995), especially near cloud edges (O'Hirok and Gautier, 2005) or at low solar elevations (Ademakinwa et al., 2024). In future work, we plan to study 1D/3D GHI retrieval errors by using data from Large Eddy Simulations in combination with 1D
550   and 3D radiative transfer as input to synthetic satellite GHI retrievals.

Code and data availability. The datasets used for the analyses and the Python codes used for preparing and post processing the CPP-SICCS data and for reproducing the presented figures are stored on the SURF Data Archive and available upon request. EUMETSAT copyrights the CPP-SICCS retrieval software and therefore it cannot be made publicly available. The SEVIRI HRIT and level 1.5 input data can be obtained from the EUMETSAT Data store at https://data.eumetsat.int/data/map/EO:EUM:DAT:MSG:MSG15-RSS (last access: 7 October 2024, Schmetz et al., 2002). The NWC SAF software can be installed by registered users from http://www.nwcsaf.org (last access: 7 October 2024, NWC SAF, 2021). LSA SAF products can be obtained by registered users from https://datalsasaf.lsasvcs.ipma.pt/PRODUCTS/MSG/MDAL/HDF5/ (last access: 7 October 2024, Carrer et al., 2018). The CAMS reanalysis and the CAMS McClear data are available from the Atmosphere Data Store at https://ads.atmosphere.copernicus.eu/datasets/cams-solar-radiation-timeseries (Gschwind et al., 2019) and https://ads.atmosphere.copernicus.eu/datasets/cams-global-reanalysis-eac4 (Inness et al., 2019). Registered users can retrieve data from the operational ECMWF archive from https://apps.ecmwf.int/archive-catalogue/ (ECMWF, 2024). The CRAAS cloud regime dataset can be retrieved from https://doi.org/10.5281/zenodo.7120267 (Tzallas et al., 2022b). The Satpy library is available from PyPI (via pip), conda-forge (via conda), or from Github. The documentation is available on: https://satpy.readthedocs.io/en/stable/index.html (last access: 9 August 2024).

Author contributions. Conceptualization of the presented work was done by JFM and JIW. The formal analysis was done by JIW, who also wrote the draft manuscript and prepared the figures. All authors were involved in regular discussions about the status of the manuscript. JFM, HD and CCvH contributed to reviewing and editing of the original manuscript. All authors have agreed upon the current version of the paper.

Competing interests. The authors declare that they have no conflict of interest.

Disclaimer. Note: Copernicus Publications remains neutral with regard to jurisdictional claims made in the text, published maps, institutional affiliations, or any other geographical representation in this paper. While Copernicus Publications makes every effort to include appropriate place names, the final responsibility lies with the authors.

575 **References**

Ademakinwa, A. S., Tushar, Z. H., Zheng, J., Wang, C., Purushotham, S., Wang, J., Meyer, K. G., Várnai, T., and Zhang, Z.: Influence of cloud retrieval errors due to three-dimensional radiative effects on calculations of broadband shortwave cloud radiative effect, Atmospheric Chemistry and Physics, 24, 3093–3114, https://doi.org/10.5194/ACP-24-3093-2024, 2024.

Alexandri, G., Georgoulias, A. K., Zanis, P., Katragkou, E., Tsikerdekis, A., Kourtidis, K., and Meleti, C.: On the ability of RegCM4 regional
580 climate model to simulate surface solar radiation patterns over Europe: An assessment using satellite-based observations, Atmospheric Chemistry and Physics, 15, 13 195–13 216, https://doi.org/10.5194/ACP-15-13195-2015, 2015.

Arbizu-Barrena, C., Ruiz-Arias, J. A., Rodríguez-Benítez, F. J., Pozo-Vázquez, D., and Tovar-Pescador, J.: Short-term solar radiation forecasting by advecting and diffusing MSG cloud index, Solar Energy, 155, 1092–1103, https://doi.org/10.1016/J.SOLENER.2017.07.045, 2017.

585 Benas, N., Solodovnik, I., Stengel, M., Huser, I., Karlsson, K. G., Hakansson, N., Johansson, E., Eliasson, S., Schroder, M., Hollmann, R., and Meirink, J. F.: CLAAS-3: The third edition of the CM SAF cloud data record based on SEVIRI observations, Earth System Science Data, 15, 5153–5170, https://doi.org/10.5194/ESSD-15-5153-2023, 2023.

Beyer, H. G., Costanzo, C., and Heinemann, D.: Modifications of the Heliosat procedure for irradiance estimates from satellite images, Solar Energy, 56, 207–212, https://doi.org/10.1016/0038-092X(95)00092-6, 1996.

590 Bieliński, T.: A Parallax Shift Effect Correction Based on Cloud Height for Geostationary Satellites and Radar Observations, Remote Sensing, 12, 365, https://doi.org/10.3390/RS12030365, 2020.

Bristor, C. L.: Central processing and analysis of geostationary satellite data, NOAA Tech. Memo. NESS 64, 155, https://api.semanticscholar.org/CorpusID:134519111, 1975.

Carrer, D., Moparthy, S., Lellouch, G., Ceamanos, X., Pinault, F., Freitas, S. C., and Trigo, I. F.: Land Surface Albedo Derived on a Ten Daily
595 Basis from Meteosat Second Generation Observations: The NRT and Climate Data Record Collections from the EUMETSAT LSA SAF, Remote Sensing 2018, Vol. 10, Page 1262, 10, 1262, https://doi.org/10.3390/RS10081262, 2018.

Chen, S., Poll, S., Franssen, H. J. H., Heinrichs, H., Vereecken, H., and Goergen, K.: Convection-Permitting ICON-LAM Simulations for Renewable Energy Potential Estimates Over Southern Africa, Journal of Geophysical Research: Atmospheres, 129, e2023JD039 569, https://doi.org/10.1029/2023JD039569, 2024.

600 Cui, Y., Wang, P., Meirink, J. F., Ntantis, N., and Wijnands, J. S.: Solar radiation nowcasting based on geostationary satellite images and deep learning models, Solar Energy, 282, 112 866, https://doi.org/10.1016/J.SOLENER.2024.112866, 2024.

de Haan, J. F., Bosma, P., and Hovenier, J.: The adding method for multiple scattering calculations of polarized light, Astronomy and astrophysics, 183, 371–391, https://ui.adsabs.harvard.edu/abs/1987A%26A...183..371D/abstract, last access: 03-07-2024, 1987.

Deneke, H., Barrientos-Velasco, C., Bley, S., Hunerbein, A., Lenk, S., Macke, A., Meirink, J. F., Schroedter-Homscheidt, M., Senf,
605 F., Wang, P., Werner, F., and Witthuhn, J.: Increasing the spatial resolution of cloud property retrievals from Meteosat SEVIRI by use of its high-resolution visible channel: Implementation and examples, Atmospheric Measurement Techniques, 14, 5107–5126, https://doi.org/10.5194/amt-14-5107-2021, 2021.

Deneke, H., Flynn, C., Foster, M., Heidinger, A., Macke, A., Meirink, J. F., Redemann, J., Sengupta, M., Walther, A., Wiltink, J., and Witthuhn, J.: Quantifying the benefits of the improved spatiotemporal resolution of current geostationary imagers for surface solar irradiance
610 retrievals based on the S2VSR campaign [Poster Abstract] (Tuesday, October 1st 2024), EUMETSAT Meteorological Satellite Conference 2024, Würzburg, Germany, https://program-eumetsat2024.kuoni-congress.info/presentation/quantifying-the-benefits-of-the-improved-s

patiotemporal-resolution-of-current-geostationary-imagers-for-surface-solar-irradiance-retrievals-based-on-the-s2vsr-campaign, last access: 24 December 2024, 2024.

Deneke, H. M. and Roebeling, R. A.: Downscaling of METEOSAT SEVIRI 0.6 and 0.8 μm channel radiances utilizing the high-resolution visible channel, Atmospheric Chemistry and Physics, 10, 9761–9772, https://doi.org/10.5194/acp-10-9761-2010, 2010.

ECMWF: ECMWF: Archive Catalogue, https://apps.ecmwf.int/archive-catalogue/, last access: 17-10-2024, 2024.

EUMETSAT: MSG Level 1.5 Image Data Format Description, EUM/MSG/ICD/105, v8 e-signed, https://user.eumetsat.int/s3/eup-strapi-media/pdf_ten_05105_msg_img_data_e7c8b315e6.pdf, last access: 01-07-2024, 2017.

Freidenreich, S. M. and Ramaswamy, V.: Analysis of the biases in the downward shortwave surface flux in the GFDL CM2.1 general circulation model, Journal of Geophysical Research Atmospheres, 116, https://doi.org/10.1029/2010JD014930, 2011.

Fritz, S., Rao, P., and Weinstein, M.: Satellite measurements of reflected solar energy and the energy received at the ground, Journal of the Atmospheric Sciences, 21, 141–151,

Fu, D., Girolamo, L. D., Rauber, R. M., McFarquhar, G. M., Nesbitt, S. W., Loveridge, J., Hong, Y., Diedenhoven, B. V., Cairns, B., Alexandrov, M. D., Lawson, P., Woods, S., Tanelli, S., Schmidt, S., Hostetler, C., and Scarino, A. J.: An evaluation of the liquid cloud droplet effective radius derived from MODIS, airborne remote sensing, and in situ measurements from CAMP2Ex, Atmospheric Chemistry and Physics, 22, 8259–8285, https://doi.org/10.5194/ACP-22-8259-2022, 2022.

Grabowski, W. W., Bechtold, P., Cheng, A., Forbes, R., Halliwell, C., Khairoutdinov, M., Lang, S., Nasuno, T., Petch, J., Tao, W. K., Wong, R., Wu, X., and Xu, K. M.: Daytime convective development over land: A model intercomparison based on LBA observations, Quarterly Journal of the Royal Meteorological Society, 132, 317–344, https://doi.org/10.1256/QJ.04.147, 2006.

Greuell, W. and Roebeling, R. A.: Toward a Standard Procedure for Validation of Satellite-Derived Cloud Liquid Water Path: A Study with SEVIRI Data, Journal of Applied Meteorology and Climatology, 48, 1575 – 1590, https://doi.org/https://doi.org/10.1175/2009JAMC2112.1, 2009.

Greuell, W., Meirink, J. F., and Wang, P.: Retrieval and validation of global, direct, and diffuse irradiance derived from SEVIRI satellite observations, Journal of Geophysical Research Atmospheres, 118, 2340–2361, https://doi.org/10.1002/jgrd.50194, 2013.

Gronemeier, T., Kanani-Sühring, F., and Raasch, S.: Do Shallow Cumulus Clouds have the Potential to Trigger Secondary Circulations Via Shading?, Boundary-Layer Meteorology, 162, 143–169, https://doi.org/10.1007/S10546-016-0180-7/FIGURES/15, 2017.

Gschwind, B., Wald, L., Blanc, P., Lefèvre, M., Schroedter-Homscheidt, M., and Arola, A.: Improving the McClear model estimating the downwelling solar radiation at ground level in cloud-free conditions – McClear-v3, Meteorologische Zeitschrift, 28, 147–163, https://doi.org/10.1127/METZ/2019/0946, (data available at: https://ads.atmosphere.copernicus.eu/datasets/cams-solar-radiation-timeseries, last access: 7 March 2024)., 2019.

Hammer, A., Heinemann, D., Lorenz, E., and Lückehe, B.: Short-term forecasting of solar radiation: a statistical approach using satellite data, Solar Energy, 67, 139–150, https://doi.org/10.1016/S0038-092X(00)00038-4, 1999.

Harsarapama, A. P., Aryani, D. R., and Rachmansyah, D.: Open-Source Satellite-Derived Solar Resource Databases Comparison and Validation for Indonesia, Journal of Renewable Energy, 2020, 1–14, https://doi.org/10.1155/2020/2134271, 2020.

Hocking, J., Vidot, J., Brunel, P., Roquet, P., Silveira, B., Turner, E., and Lupu, C.: A new gas absorption optical depth parameterisation for RTTOV version 13, Geoscientific Model Development, 14, 2899–2915, https://doi.org/10.5194/GMD-14-2899-2021, 2021.

Holmlund, K., Grandell, J., Schmetz, J., Stuhlmann, R., Bojkov, B., Munro, R., Lekouara, M., Coppens, D., Viticchie, B., August, T., Theodore, B., Watts, P., Dobber, M., Fowler, G., Bojinski, S., Schmid, A., Salonen, K., Tjemkes, S., Aminou, D., and Blythe, P.: Meteosat

Third Generation (MTG): Continuation and Innovation of Observations from Geostationary Orbit, Bulletin of the American Meteorological Society, 102, E990–E1015, https://doi.org/10.1175/BAMS-D-19-0304.1, 2021.

650 Huang, G., Li, Z., Li, X., Liang, S., Yang, K., Wang, D., and Zhang, Y.: Estimating surface solar irradiance from satellites: Past, present, and future perspectives, Remote Sensing of Environment, 233, https://doi.org/10.1016/j.rse.2019.111371, 2019.

Inness, A., Ades, M., Agustí-Panareda, A., Barr, J., Benedictow, A., Blechschmidt, A. M., Dominguez, J. J., Engelen, R., Eskes, H., Flemming, J., Huijnen, V., Jones, L., Kipling, Z., Massart, S., Parrington, M., Peuch, V. H., Razinger, M., Remy, S., Schulz, M., and Suttie, M.: The CAMS reanalysis of atmospheric composition, Atmospheric Chemistry and Physics, 19, 3515–3556, https://doi.org/10.5194/ACP-19-3515-2019, (data available at: https://ads.atmosphere.copernicus.eu/datasets/cams-global-reanalysis-eac4, last access: 7 March 2024)., 2019.

Jakub, F. and Mayer, B.: The role of 1-D and 3-D radiative heating in the organization of shallow cumulus convection and the formation of cloud streets, Atmospheric Chemistry and Physics, 17, 13 317–13 327, https://doi.org/10.5194/ACP-17-13317-2017, 2017.

660 Journée, M., Stöckli, R., and Bertrand, C.: Sensitivity to spatio-temporal resolution of satellite-derived daily surface solar irradiation, Remote Sensing Letters, 3, 315–324, https://doi.org/10.1080/01431161.2011.593579, 2012.

Karlsson, K. G. and Devasthale, A.: Inter-Comparison and Evaluation of the Four Longest Satellite-Derived Cloud Climate Data Records: CLARA-A2, ESA Cloud CCI V3, ISCCP-HGM, and PATMOS-x, Remote Sensing 2018, Vol. 10, Page 1567, 10, 1567, https://doi.org/10.3390/RS10101567, 2018.

665 Li, J., Huang, J., Stamnes, K., Wang, T., Lv, Q., and Jin, H.: A global survey of cloud overlap based on CALIPSO and CloudSat measurements, Atmos. Chem. Phys, 15, 519–536, https://doi.org/10.5194/acp-15-519-2015, 2015.

Lorenzo, A. T., Morzfeld, M., Holmgren, W. F., and Cronin, A. D.: Optimal interpolation of satellite and ground data for irradiance nowcasting at city scales, Solar Energy, 144, 466–474, https://doi.org/10.1016/J.SOLENER.2017.01.038, 2017.

Macke, A., Seifert, P., Baars, H., Barthlott, C., Beekmans, C., Behrendt, A., Bohn, B., Brueck, M., Bühl, J., Crewell, S., Damian, T., Deneke, H., Düsing, S., Foth, A., Girolamo, P. D., Hammann, E., Heinze, R., Hirsikko, A., Kalisch, J., Kalthoff, N., Kinne, S., Kohler, M., Löhnert, U., Madhavan, B. L., Maurer, V., Muppa, S. K., Schween, J., Serikov, I., Siebert, H., Simmer, C., Späth, F., Steinke, S., Träumner, K., Trömel, S., Wehner, B., Wieser, A., Wulfmeyer, V., and Xie, X.: The HD(CP)2 Observational Prototype Experiment (HOPE) - An overview, Atmospheric Chemistry and Physics, 17, 4887–4914, https://doi.org/10.5194/ACP-17-4887-2017, 2017.

Madhavan, B. L., Kalisch, J., and Macke, A.: Shortwave surface radiation network for observing small-scale cloud inhomogeneity fields, 675 Atmospheric Measurement Techniques, 9, 1153–1166, https://doi.org/10.5194/amt-9-1153-2016, 2016.

Marie-Joseph, I., Linguet, L., Gobinddass, M. L., and Wald, L.: On the applicability of the Heliosat-2 method to assess surface solar irradiance in the Intertropical Convergence Zone, French Guiana, International Journal of Remote Sensing, 34, 3012–3027, https://doi.org/10.1080/01431161.2012.756598, 2013.

Marshak, A., Davis, A., Wiscombe, W., and Titov, G.: The verisimilitude of the independent pixel approximation used in cloud remote 680 sensing, Remote Sensing of Environment, 52, 71–78, https://doi.org/10.1016/0034-4257(95)00016-T, 1995.

Marshak, A., Platnick, S., Várnai, T., Wen, G., and Cahalan, R. F.: Impact of three-dimensional radiative effects on satellite retrievals of cloud droplet sizes, Journal of Geophysical Research Atmospheres, 111, https://doi.org/10.1029/2005JD006686, 2006.

Matar, C., Cornet, C., Parol, F., Labonnote, L. C., Auriol, F., and Nicolas, M.: Liquid cloud optical property retrieval and associated uncertainties using multi-angular and bispectral measurements of the airborne radiometer OSIRIS, Atmospheric Measurement Techniques, 16, 685 3221–3243, https://doi.org/10.5194/AMT-16-3221-2023, 2023.

Miller, S. D., Rogers, M. A., Haynes, J. M., Sengupta, M., and Heidinger, A. K.: Short-term solar irradiance forecasting via satellite/model coupling, Solar Energy, 168, 102–117, https://doi.org/10.1016/J.SOLENER.2017.11.049, 2018.

Mood, A.: Introduction to the Theory of Statistics, McGraw-Hill, 1950.

Munneke, P. K., Reijmer, C. H., van den Broeke, M. R., König-Langlo, G., Stammes, P., and Knap, W. H.: Analysis of clear-sky Antarc-
690   tic snow albedo using observations and radiative transfer modeling, Journal of Geophysical Research: Atmospheres, 113, 17 118, https://doi.org/10.1029/2007JD009653, 2008.

Nakajima, T. and King, M. D.: Determination of the Optical Thickness and Effective Particle Radius of Clouds from Reflected Solar Radiation Measurements. Part I: Theory, Journal of Atmospheric Sciences, 47, 1878 – 1893, https://doi.org/10.1175/1520-0469(1990)047<1878:DOTOTA>2.0.CO;2, 1990.

695   NWC SAF: Algorithm Theoretical Basis Document for Cloud Product Processors of the NWC/GEO (GEO-CMA-v5.1 (NWC-009), GEO-CT-v4.1 (NWC-016), GEO-CTTH-v4.1 (NWC-017) and GEO CMIC-v2.1 (NWC-021), https://www.nwcsaf.org/Downloads/GEO/2021/Documents/Scientific_Docs/NWC-CDOP3-GEO-MFL-SCI-ATBD-Cloud_v1.0.1.pdf, last access: 01-07-2024, 2021.

O'Hirok, W. and Gautier, C.: The Impact of Model Resolution on Differences between Independent Column Approximation and Monte Carlo Estimates of Shortwave Surface Irradiance and Atmospheric Heating Rate, Journal of the Atmospheric Sciences, 62, 2939–2951,
700   https://doi.org/10.1175/JAS3519.1, 2005.

Ohtake, H., Uno, F., Oozeki, T., Yamada, Y., Takenaka, H., and Nakajima, T. Y.: Estimation of satellite-derived regional photovoltaic power generation using a satellite-estimated solar radiation data, Energy Science and Engineering, 6, 570–583, https://doi.org/10.1002/ese3.233, 2018.

Perez, R., Kivalov, S., Schlemmer, J., Hemker, K., Renné, D., and Hoff, T. E.: Validation of short and medium term operational solar radiation
705   forecasts in the US, Solar Energy, 84, 2161–2172, https://doi.org/10.1016/J.SOLENER.2010.08.014, 2010.

Qu, Z., Oumbe, A., Blanc, P., Espinar, B., Gesell, G., Gschwind, B., Klüser, L., Lefèvre, M., Saboret, L., Schroedter-Homscheidt, M., and Wald, L.: Fast radiative transfer parameterisation for assessing the surface solar irradiance: The Heliosat-4 method, Meteorologische Zeitschrift, 26, 33–57, https://doi.org/10.1127/METZ/2016/0781, 2017.

Roy, A., Hammer, A., Heinemann, D., Schroedter-Homscheidt, M., Lünsdorf, O., and Lezaca, J.: Revisiting Parallax and Cloud Shadow
710   Correction in Satellite-Based Solar Irradiance Estimation, SSRN, https://doi.org/https://dx.doi.org/10.2139/ssrn.4630664, 2024-Preprint.

Satpy Developers: Satpy Documentation Release 0.49.1.dev0+g7b2e5a7fc.d20240605, https://satpy.readthedocs.io/_/downloads/en/v0.49.0/pdf/, last access: 29-07-2024, 2024.

Saunders, R., Hocking, J., Turner, E., Rayer, P., Rundle, D., Brunel, P., Vidot, J., Roquet, P., Matricardi, M., Geer, A., Bormann, N., and Lupu, C.: An update on the RTTOV fast radiative transfer model (currently at version 12), Geoscientific Model Development, 11, 2717–2737,
715   https://doi.org/10.5194/GMD-11-2717-2018, 2018.

Schmetz, J., Paolo, P., Tjemkes, S., Just, D., Kerkman, J., Rota, S., and Ratier, A.: An Introduction to Meteosat Second Generation (MSG), Bulletin of the American Meteorological Society, 83, 977–992,

Schmit, T. J., Griffith, P., Gunshor, M. M., Daniels, J. M., Goodman, S. J., and Lebair, W. J.: A Closer Look at the ABI on the GOES-R Series, Bulletin of the American Meteorological Society, 98, 681–698, https://doi.org/10.1175/BAMS-D-15-00230.1, 2017.

720   Stammes, P.: IRS 2000: Current Problems in Atmospheric Radiation, A. Deepak Publ., Hampton, VA, pp. 385–388, 2001.

Tarpley, J. D.: Estimating incident solar radiation at the surface from geostationary satellite data., Journal of Applied Meteorology, 18, 1172 – 1181, https://doi.org/10.1175/1520-0450(1979)018<1172:EISRAT>2.0.CO;2, 1979.

Tzallas, V., Hünerbein, A., Stengel, M., Meirink, J. F., Benas, N., Trentmann, J., and Macke, A.: CRAAS: A European Cloud Regime dAtAset Based on the CLAAS-2.1 Climate Data Record, Remote Sensing, 14, https://doi.org/10.3390/RS14215548, 2022a.

725 Tzallas, V., Hünerbein, A., Stengel, M., Meirink, J. F., Benas, N., Trentmann, J., and Macke, A.: CRAAS: Cloud Regime dAtAset based on the CLAAS-2.1 climate data record, Zenodo [dataset], https://doi.org/10.5281/zenodo.7120267, 2022b.

Urraca, R., Lanconelli, C., and Gobron, N.: Impact of the Spatio-Temporal Mismatch Between Satellite and In Situ Measurements on Validations of Surface Solar Radiation, Journal of Geophysical Research: Atmospheres, 129, https://doi.org/10.1029/2024JD041007, 2024.

Veerman, M. A., Pedruzo-Bagazgoitia, X., Jakub, F., de Arellano, J. V.-G., and van Heerwaarden, C. C.: Three-Dimensional Radiative Effects
730 By Shallow Cumulus Clouds on Dynamic Heterogeneities Over a Vegetated Surface, Journal of Advances in Modeling Earth Systems, 12, e2019MS001 990, https://doi.org/10.1029/2019MS001990, 2020.

Vonderhaar, T. and Suomi, V.: Satellite Observations of the Earth's Radiation Budget, https://doi.org/https://doi.org/10.1126/science.163.3868.667, 1969.

Wang, P., van Westrhenen, R., Meirink, J. F., van der Veen, S., and Knap, W.: Surface solar radiation forecasts by
735 advecting cloud physical properties derived from Meteosat Second Generation observations, Solar Energy, 177, 47–58, https://doi.org/10.1016/j.solener.2018.10.073, 2019.

Wiltink, J. I., Deneke, H., Saint-Drenan, Y.-M., Heerwaarden, C. C. V., and Meirink, J. F.: Validating global horizontal irradiance retrievals from Meteosat SEVIRI at increased spatial resolution against a dense network of ground-based observations, Atmos. Meas. Tech., 17, 6003–6024, https://doi.org/https://doi.org/10.5194/amt-17-6003-2024, 2024.

740 Wyser, K., O'Hirok, W., Gautier, C., and Jones, C.: Remote sensing of surface solar irradiance with corrections for 3-D cloud effects, Remote Sensing of Environment, 80, 272–284, https://doi.org/10.1016/S0034-4257(01)00309-1, 2002.

Yagli, G. M., Yang, D., Gandhi, O., and Srinivasan, D.: Can we justify producing univariate machine-learning forecasts with satellite-derived solar irradiance?, Applied Energy, 259, 114 122, https://doi.org/10.1016/J.APENERGY.2019.114122, 2020.

Zhang, Z., Ackerman, A. S., Feingold, G., Platnick, S., Pincus, R., and Xue, H.: Effects of cloud horizontal inhomogeneity and drizzle
745 on remote sensing of cloud droplet effective radius: Case studies based on large-eddy simulations, Journal of Geophysical Research: Atmospheres, 117, 19 208, https://doi.org/10.1029/2012JD017655, 2012.

Zinner, T. and Mayer, B.: Remote sensing of stratocumulus clouds: Uncertainties and biases due to inhomogeneity, Journal of Geophysical Research: Atmospheres, 111, 14 209, https://doi.org/10.1029/2005JD006955, 2006.